

Experimental and theoretical investigations of the photoelectrochemical and photo-Fenton properties of Co-doped FeOCl

Jin-Huan Ma(马金环), Zhi-Qiang Wei(魏智强), Mei-Jie Ding(丁梅杰), Ji-Wei Zhao(赵继威), and Cheng-Gong Lu(路承功)

Citation: Chin. Phys. B, 2023, 32 (**9**): 097202. DOI: 10.1088/1674-1056/acae7f
Journal homepage: http://cpb.iphy.ac.cn; http://iopscience.iop.org/cpb

What follows is a list of articles you may be interested in

Thickness-dependent exciton relaxation dynamics of few-layer rhenium diselenide

Chang-Fu Huo(霍唱福), Tiantian Yun(云田田), Xiao-Qing Yan(鄢小卿), Zewen Liu(刘泽文), Xin Zhao(赵欣), Wenxiong Xu(许文雄), Qiannan Cui(崔乾楠), Zhi-Bo Liu(刘智波), and Jian-Guo Tian(田建国)

Chin. Phys. B, 2023, 32 (**6**): 067203. DOI: 10.1088/1674-1056/acc1d3

A novel monoclinic phase and electrically tunable magnetism of van der Waals layered magnet $CrTe_2$

Qidi Ren(任启迪), Kang Lai(赖康), Jiahao Chen(陈家浩), Xiaoxiang Yu(余晓翔), and Jiayu Dai(戴佳钰)

Chin. Phys. B, 2023, 32 (**2**): 027201. DOI: 10.1088/1674-1056/ac9b37

Observation of large in-plane anisotropic transport in van der Waals semiconductor Nb_2SiTe_4

Kaiyao Zhou(周楷尧), Jun Deng(邓俊), Long Chen(陈龙), Wei Xia(夏威), Yanfeng Guo(郭艳峰), Yang Yang(杨洋), Jian-Gang Guo(郭建刚), and Liwei Guo(郭丽伟)

Chin. Phys. B, 2021, 30 (**8**): 087202. DOI: 10.1088/1674-1056/ac068f

Effect of strain on exciton dynamics in monolayer WS_2

Lu Zhang(张璐), Da-Wei He(何大伟), Jia-Qi He(何家琪), Yang Fu(付洋), Yong-Sheng Wang(王永生)

Chin. Phys. B, 2019, 28 (**8**): 087201. DOI: 10.1088/1674-1056/28/8/087201

Effect of Nb doping on microstructures and thermoelectric properties of $SrTiO_3$ ceramics

Da-Quan Liu(刘达权), Yu-Wei Zhang(张玉伟), Hui-Jun Kang(康慧君), Jin-Ling Li(李金玲), Xiong Yang(杨雄), Tong-Min Wang(王同敏)

Chin. Phys. B, 2018, 27 (**4**): 047205. DOI: 10.1088/1674-1056/27/4/047205

Experimental and theoretical investigations of the photoelectrochemical and photo-Fenton properties of Co-doped FeOCl

Jin-Huan Ma(马金环)[1], Zhi-Qiang Wei(魏智强)[1,2,†], Mei-Jie Ding(丁梅杰)[1], Ji-Wei Zhao(赵继威)[1], and Cheng-Gong Lu(路承功)[1]

[1] *School of Science, Lanzhou University of Technology, Lanzhou* 730050, *China*

[2] *State Key Laboratory of Advanced Processing and Recycling of Non-ferrous Metals, Lanzhou University of Technology, Lanzhou* 730050, *China*

(Received 24 October 2022; revised manuscript received 19 December 2022; accepted manuscript online 27 December 2022)

For the first time, two-dimensional FeOCl ($Fe_{1-x}Co_xOCl$) doped with Co was successfully applied to the photocatalytic and photo-Fenton degradation of Rhodamine B (RhB). The photocatalytic and photo-Fenton experiments showed that the degradation rates of RhB by $Fe_{0.94}Co_{0.06}OCl$ are 82.6% and 98.2% within 50 min under neutral solution, room temperature and visible light. The inclusion of Co resulted in lattice imperfections on the surface of FeOCl, which was advantageous for the photogenerated electron–hole pair separation efficiency (consistent with the density functional theory calculation). Moreover, the RhB removal rate decreased from 98% to 82% during five successive cycles, showing good structural stability. Finally, based on the radical capture experiment, a potential mechanism for RhB degradation by $Fe_{1-x}Co_xOCl$ catalyst was proposed. The idea of a synergistic mechanism for $Fe_{1-x}Co_xOCl$ also offers a fresh concept for catalysts used in doping modification.

Keywords: Co doped FeOCl, photo-Fenton, photocatalytic, DFT calculations

PACS: 72.80.Ga, 78.40.–q, 81.07.–b, 68.37.lp **DOI:** 10.1088/1674-1056/acae7f

1. Introduction

Nowadays, water pollution is a global issue that affects all nations.[1,2] Various synthetic organic dyes are discharged into wastewater and eventually into natural water bodies, and most of these compounds are persistent organic compounds.[3,4] Water pollution caused by persistent organic pollutants (POPs) is one of the most challenging large-scale problems of the 21st century.[5–7] This organic wastewater is highly harmful to human health and the aqueous environment, but these compounds are very difficult to naturally degrade or eliminate.[8,9] Due to its high toxicity, stability and biological persistence, Rhodamine B (RhB) can hinder plant growth and is one of the three main types of carcinogen produced by the textile industry.[10,11] Different wastewater treatment approaches, such as adsorption, coagulation and precipitation, have been suggested to lessen the environmental impact of POPs in water; however, these approaches only appear to transfer POPs from one phase to another.[12,13] Compared with these methods, a photo-Fenton reaction can degrade pollutants in water faster and more efficiently during wastewater treatment.[8,14] Throughout this process, H_2O_2 stimulates the Fe^{2+}/Fe^{3+} cycle and generates a significant number of ·OH radicals to efficiently degrade pollutants in water.[15,16] The degradation of persistent contaminants has drawn increasing attention to the photo-Fenton reaction.[17,18] Therefore, the development of photo-Fenton catalysts is highly significant from an economic and environmental perspective.[19,20]

In recent years, more and more Fe-based Fenton catalysts have been reported.[21] Gao *et al.*[22] successfully synthesized the Z-type heterostructure of the α-Fe_2O_3@g-C_3N_4 catalyst through co-calcination of melamine and iron-based metal–organic frameworks. This catalyst exhibits excellent photo-Fenton performance and high stability over a wide pH range. To address the issues of weak conductivity, easy aggregation and high optoelectronic recombination rate of Fe–Ni layered double metal hydroxide (FeNi-LDH), Yang *et al.*[23] created FeNi-LDH/Ti_3C_2. Therefore, developing the excellent photo-Fenton performance of iron-based catalysts has always been a key project in the fields of materials science and wastewater remediation. Moreover, defects caused by doping are also an effective method to modify a material. According to Yang *et al.*,[24] inherent flaws can frequently reveal more active sites, enhance conductivity, adjust the electronic state and promote ion diffusion, all of which can effectively improve catalytic performance. Sun *et al.*[25] demonstration of oxygen vacancy-rich vanadium-doped Co_3O_4 emphasized the importance of heteroatoms and defects as a means of enhancing a material's properties.

In this study, we combine experimental techniques with density functional theory (DFT) computations and propose the doping of Co into FeOCl, which is an orthorhombic narrow-bandgap (1.8 eV) semiconductor. The doping of the transition metal Co mainly provides more ion capture centers for

†Corresponding author. E-mail: qianweizuo@163.com

© 2023 Chinese Physical Society and IOP Publishing Ltd

the catalyst, effectively separates electron–hole pairs, causes lattice defects and introduces impurity energy levels so that smaller energies can also excite electrons and expand the photoresponse range. Combined with density functional DFT calculations, the optimal geometric state, band structure and density of states distribution of surface atoms were determined.

2. Materials and methods

2.1. Synthesis of $Fe_{1-x}Co_xOCl$ composites

All the chemicals used in this study were analytically pure, including ferric chloride hexahydrate ($FeCl_3 \cdot 6H_2O$, $\geq$ 99%), cobalt nitrate hexahydrate ($Co(NO_3)_2 \cdot 6H_2O$, $\geq$ 99%), ethanol (C_2H_6O, $\geq$ 99.7%), propan-2-ol [$C_4H_{10}O$ (IPA), $\geq$ 98.0%], acetone (C_3H_6O, $\geq$ 99.5%), methanol [CH_4O (IA), $\geq$ 99%], 1,4-benzoquinone [$C_6H_4O_2$ (BQ), $\geq$ 99%] and hydrogen peroxide (H_2O_2, $\geq$ 99.5%), and no further purification was required for use. As shown in Fig. 1, the $Fe_{1-x}Co_xOCl$ composite was synthesized by a simple one-step calcination method. First, three equal portions of 2 g of $FeCl_3 \cdot 6H_2O$ were weighed, followed by 0.12 g, 0.28 g and 0.4 g of $Co(NO_3)_2 \cdot 6H_2O$, respectively. The two were dissolved in 5 ml H_2O and sonicated for 30 min, then dried in a drying oven at 60 °C for 12 h to evaporate the excess solvent. The dry solid was then heated in a muffle furnace to 250 °C at a rate of 5 °C·min^{-1} and kept for 1 h. After natural cooling to room temperature, the solids were taken out and washed several times with C_3H_6O to remove excess $FeCl_3$. The reddish-black powders obtained after drying were named $Fe_{0.97}Co_{0.03}OCl$, $Fe_{0.94}Co_{0.06}OCl$ and $Fe_{0.90}Co_{0.10}OCl$, respectively.

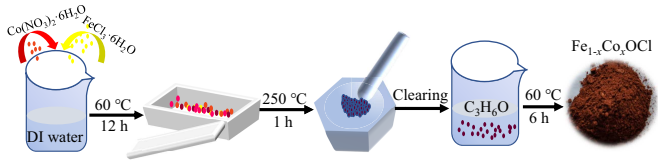


Fig. 1. Schematic illustration of the synthesis of $Fe_{1-x}Co_xOCl$.

2.2. Characterization

The functional groups of inorganic materials were characterized using a variety of techniques, including x-ray diffraction (XRD; Rigaku, Japan, D/Max-2400) with Cu K radiation in the angle range of 10°–80°, scanning electron microscopy with a scanning rate of 0.2°·s^{-1} and a step size of 0.02° , field emission scanning electron microscopy (FESEM; 200FEG), high-resolution transmission electron microscopy (HRTEM; JEM-2010) and Fourier transform infrared (FT-IR) spectroscopy. The chemical state of elements on the material surface was assessed using x-ray photoelectron spectroscopy (XPS; PHI-5702), while a fluorophotometer was used for photoluminescence (PL) spectroscopy. A TU-1901 spectrophotometer was used to measure the UV–visible absorption spectrum.

2.3. Catalytic activity measurement and radical-trapping experiment

In a typical photocatalytic experiment, 100 ml of neutral RhB solution containing 10 mg·l^{-1} of catalyst was used. To get the solution to the adsorption and desorption equilibrium it was left for 30 min absorbing in the dark. After turning on the xenon lamp (VS-GCH-XE-300), 5 ml of the mixed solution was taken every 5 min to measure the absorbance with a UV spectrophotometer. Similar to this, without altering any conditions, 0.5 ml of H_2O_2 was added to the solution before turning on the xenon lamp to perform the photo-Fenton experiment. By including IPA, BQ and IA in the radical trapping experiment, the active compounds impacting the photo-Fenton reaction were investigated. Furthermore, the composites were subjected to five-cycle stability photo-Fenton tests.

2.4. DFT calculations

All the spin-polarized calculations were performed using the CASTEP program with the generalized gradient approximation and the Perdew–Burke–Ernzerhof exchange-correlation functional.[26] As shown in Fig. 2, FeOCl crystal has a layered structure and its primitive bulk unit contains Fe, O and Cl atoms. The optimized lattice parameters are $a = 0.3330$ nm, $b = 0.8360$ nm and $c = 0.3860$ nm, in agreement with the values on the XRD characterization standard card JCPDS 72-0619 ($a = 0.3780$ nm, $b = 0.7917$ nm, $c = 0.3302$ nm). The Brillouin zone was sampled using the ORC lattice with the following path: C–X–S–Y–C–Z–U–R–T–$Z|Y$–$T|U$–$X|S$–R.[27]

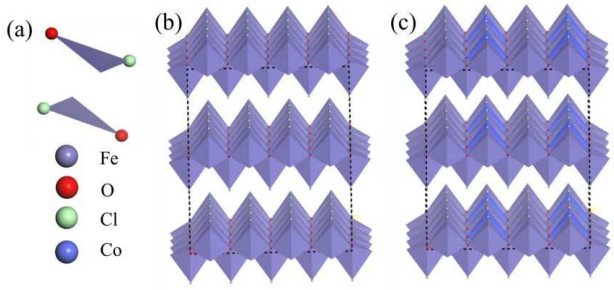


Fig. 2. Structure of a primitive bulk unit (a), supercell of FeOCl crystal (b) and supercell of Co doped FeOCl crystal (c).

3. Results and discussion

3.1. Crystal structure and morphological analysis

According to the XRD patterns of all samples in Fig. 3(a), the orthogonal FeOCl (JCPDS 72-0619) crystal planes (010), (110), (021), (111), (200), (131), (002) and (022) are represented by diffraction peaks at $2\theta = 11.05°$, 26.03°, 35.45°, 38.10°, 48.10° and 60.89° in the Co-doped FeOCl species. It demonstrates that following Co doping, the FeOCl crystal structure remained unchanged, and no additional immediately apparent distinctive peaks were discovered, demonstrating the extremely high degree of purity of the samples used. However,

because $Co(NO_3)_2$ is acidic after hydrolysis, the intensity of the diffraction peak is obviously weakened, which may be related to the environment of $FeCl_3$ before calcination. When the peaks are at $2\theta = 26.03°$ and 35.45°, the diffraction peaks are gradually intensified as the amount of doping increases, and the diffraction peaks of all doped samples are broadened compared with the undoped samples. This may be caused by lattice distortion due to Co doping. However, the diffraction peaks of $Fe_{1-x}Co_xOCl$ shifted to bigger angles than those of FeOCl (Fig. 3(b)), illustrating the incorporation of Co into the FeOCl lattice.

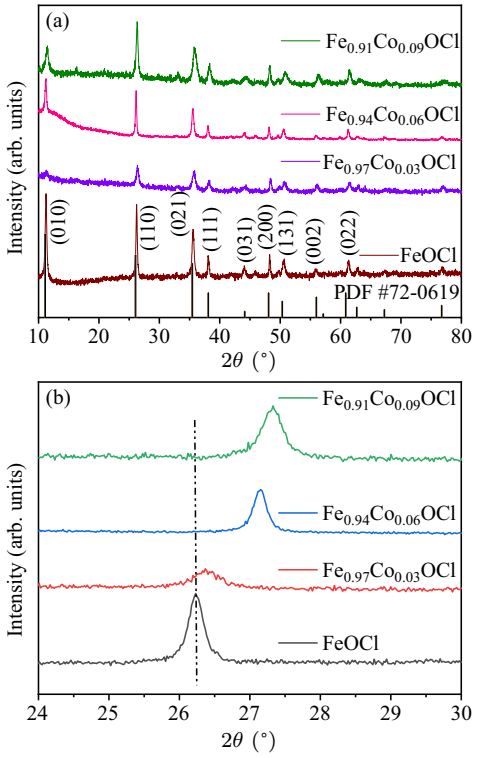


Fig. 3. (a) and (b) XRD patterns and diffraction peaks of $Fe_{1-x}Co_xOCl$.

SEM was used to determine the morphology of the synthesized material. As seen in Fig. 4(a), pure FeOCl demonstrated an obvious irregular sheet stack structure. The SEM image of the $Fe_{0.94}Co_{0.06}OCl$ nanosheet is compared with pure FeOCl to show the effect of Co doping in Fig. 4(b). It is found that the doped sample possesses a rough surface and nanosheets.

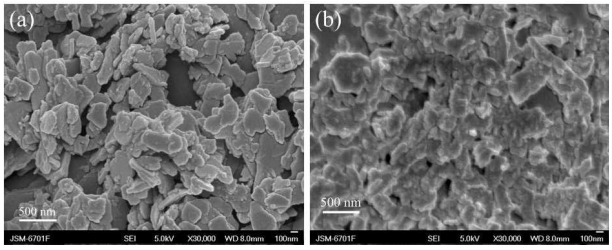


Fig. 4. SEM images of (a) FeOCl and (b) $Fe_{0.94}Co_{0.06}OCl$.

Figure 5 was used to further explore the morphology and shows lattice changes of Co-doped FeOCl compared with pure FeOCl. The TEM images of pure FeOCl and $Fe_{0.94}Co_{0.06}OCl$ are consistent with the SEM image, as shown in Figs. 5(a) and 5(c), while Figs. 5(b) and 5(d) show the HRTEM images of pure FeOCl and $Fe_{0.94}Co_{0.06}OCl$ samples, respectively. The interplanar distance of $Fe_{0.94}Co_{0.06}OCl$ (0.190 nm) with clear lattice fringes is greater than that of pure FeOCl (0.188 nm), demonstrating that the crystal lattice tends to expand as a result of the different metal ion radii. It is evident from the interpolated chosen electron diffraction pattern that FeOCl is a single crystal and that doping with Co causes the diffraction spot to change into a diffraction ring. Diffraction rings (inner to outer) are consistent with those of the FeOCl structure in XRD. In short, Co was successfully doped into FeOCl.

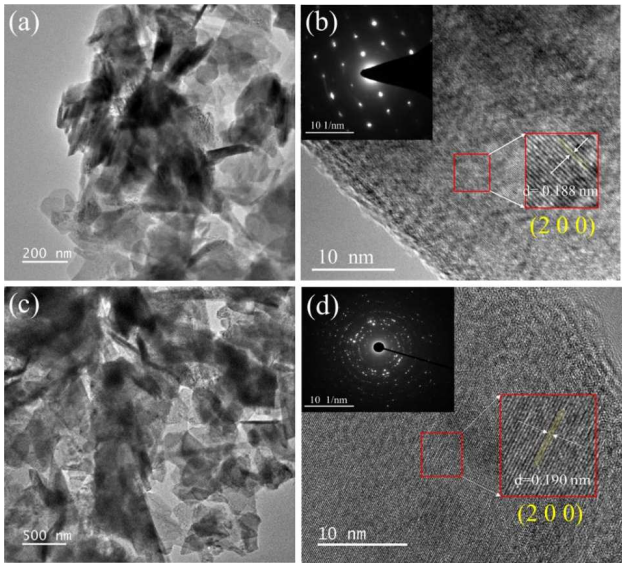


Fig. 5. TEM and HRTEM images of [(a) and (b)] FeOCl and [(c) and (d)] $Fe_{0.94}Co_{0.06}OCl$.

To get the elemental composition of the sample, we tested the energy-dispersive x-ray (EDS) spectrum as shown in Fig. 6(a). $Fe_{0.94}Co_{0.06}OCl$ contains three main elements (Fe, O and Cl), but it can also be observed that the characteristic peak of the doped element Co is located at 2.86 keV. The presence of Co can also be seen from TEM mapping (Figs. 6(c)–6(f)). It can be seen that the elements are evenly distributed and there is no enrichment.

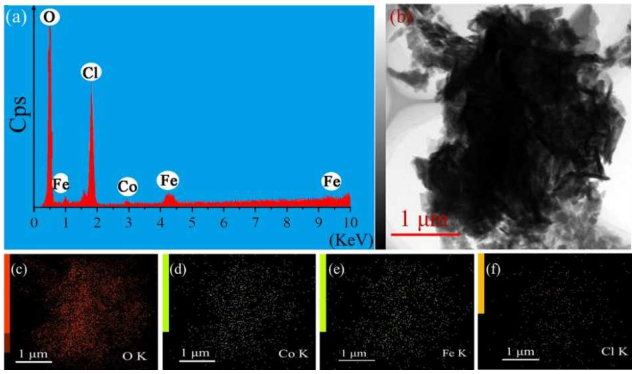


Fig. 6. (a) EDS pattern and (c)–(f) the corresponding element mappings for $Fe_{0.94}Co_{0.06}OCl$.

3.2. Optical properties

XPS was used to characterize the composition and chemical state of the material surface, and all XPS data were adjusted by 284.8 eV for C 1s.[28] The complete XPS spectrum of Fe, O and Cl elements found in FeOCl and $Fe_{0.94}Co_{0.06}OCl$ is shown in Fig. 7(a). It was found that Co 2p replaces Fe 2s in the full spectrum of $Fe_{0.94}Co_{0.06}OCl$. The satellite peak of Fe 2p is shown in Fig. 7(b), with peak locations at 711.4 eV and 725.2 eV, respectively, for Fe $2p_{3/2}$ and Fe $2p_{1/2}$ of $Fe_{0.94}Co_{0.06}OCl$.[29,30] The lower binding energy of Fe 2p in $Fe_{0.94}Co_{0.06}OCl$ compared with FeOCl indicates the reduction of the valence state Fe^{3+} in $Fe_{0.94}Co_{0.06}OCl$.[31] The O 1s peak appears between 531.5 eV and 530.5 eV in Fig. 7(c), while the peak at 530.5 eV matches the Fe–O or Co–O in $Fe_{0.94}Co_{0.06}OCl$. The peak at 531.5 eV and other O peaks are attributed to H_2O and ·OH.[32,33] Figure 7(d) shows the XPS spectrum of Co 2p where the peak position appears at 798.0 eV and 783.4 eV to match Co $2p_{1/2}$ or Co $2p_{3/2}$ of metal Co.[34] Among them, the peak at 783.4 eV is the satellite peak of Co^{3+} and the peak at 798.0 eV is the satellite peaks of Co^{2+}, indicating that Co exists in the state of Co^{2+} and Co^{3+} in the composite material. The spectrum of Cl 2p in Fig. 7(e) reveals that the peaks at 198.8 eV and 200.0 eV may be related to the Fe–Cl or Co–Cl bonds of $Fe_{0.94}Co_{0.06}OCl$.[35] The XPS results proved that Co was successfully incorporated into FeOCl.

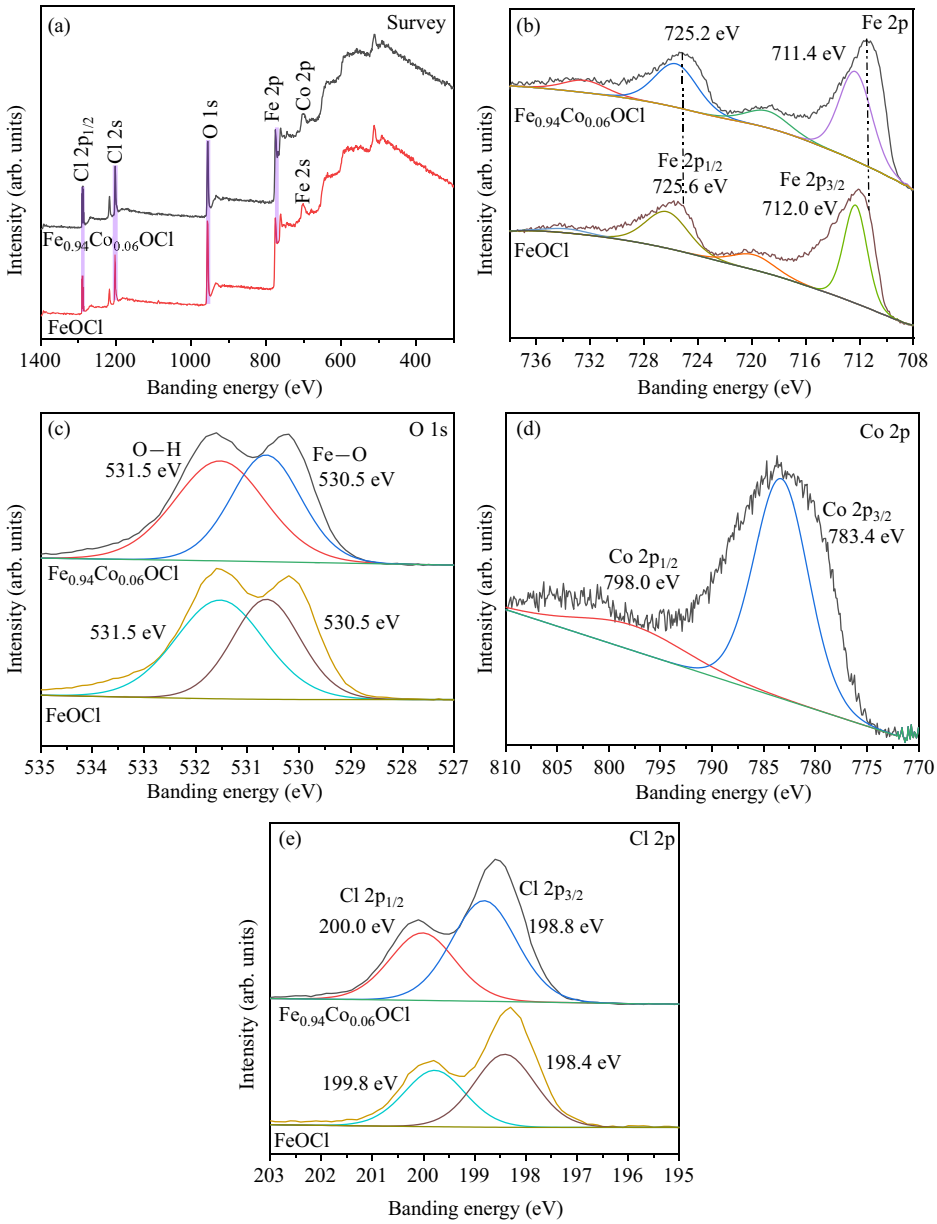


Fig. 7. High resolution XPS: (a) survey spectra, (b) Fe 2p, (c) O 1s, (d) Co 2p and (e) Cl 2p of FeOCl and $Fe_{0.94}Co_{0.06}OCl$.

FT-IR was used to characterize the functional groups of materials and the scan range was 400 cm^{-1}–4000 cm^{-1}. The bending and stretching modes of O–H and H–O–H induced by H_2O adsorbed on the surface of the material can be seen in Fig. 8 with a wide and smooth strong absorption peak appearing at 3300 cm^{-1}–1600 cm^{-1}.[36,37] The peak at 1500 cm^{-1}–

1600 cm^{-1} can be attributed to ethanol or chemical substances added during test preparation.[38] At 814 cm^{-1}, the bending vibration of OH was also noticed. The Fe–O peak of the changed material at 496 cm^{-1} exhibits a clear redshift when compared with pure FeOCl. This redshift is brought on by the vibration of Fe–O–Co and demonstrates that Co and FeOCl are involved in the interaction.[36–38] The bending vibration of OH was also observed at 814 cm^{-1}. Compared with pure FeOCl, the Fe–O peak of the modified material at 496 cm^{-1} undergoes an obvious redshift, which is caused by the vibration of Fe–O–Co, showing there is interaction between Co and FeOCl.[36]

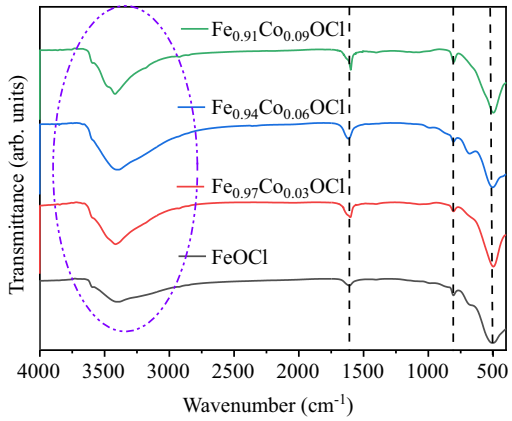


Fig. 8. FT-IR spectra of $Fe_{1-x}Co_xOCl$.

The light absorption capacity of a catalyst has an important effect on its catalytic activity.[39] The visible light absorption spectra of $Fe_{1-x}Co_xOCl$ composites are shown in Figs. 9(a)–9(d), and it was discovered that the composite had a broad absorption band between 500 nm and 700 nm and a short absorption tail at 750 nm. Compared with pure FeOCl, the absorption intensity of the composite sample is obviously improved in the range of 500 nm–700 nm, and the absorption edge redshift is in the range of 500 nm–700 nm. This indicates that Co doping in FeOCl can enhance the response range in the visible light region. Additionally, the Tauc formula is used to determine the material's semiconductor bandgap value[40]

$$(\alpha h\nu)^{1/n} = A(h\nu - E_g). \tag{1}$$

where n depends on the type of semiconductor. $Fe_{1-x}Co_xOCl$ composite semiconductor materials are indirect bandgap semiconductors (obtained from the band structure calculated by DFT). Therefore, it is further concluded that the bandgaps of FeOCl, $Fe_{0.97}Co_{0.03}OCl$, $Fe_{0.94}Co_{0.06}OCl$ and $Fe_{0.90}Co_{0.10}OCl$ nanosheet in Table 1 are 1.80 eV, 1.76 eV, 1.71 eV and 1.68 eV, respectively, indicating that the semiconductor bandgap is reduced after modification, broadening the light absorption range. This could be the result of doping, which raises the bandgap impurity levels and affects the electronic structure.[41]

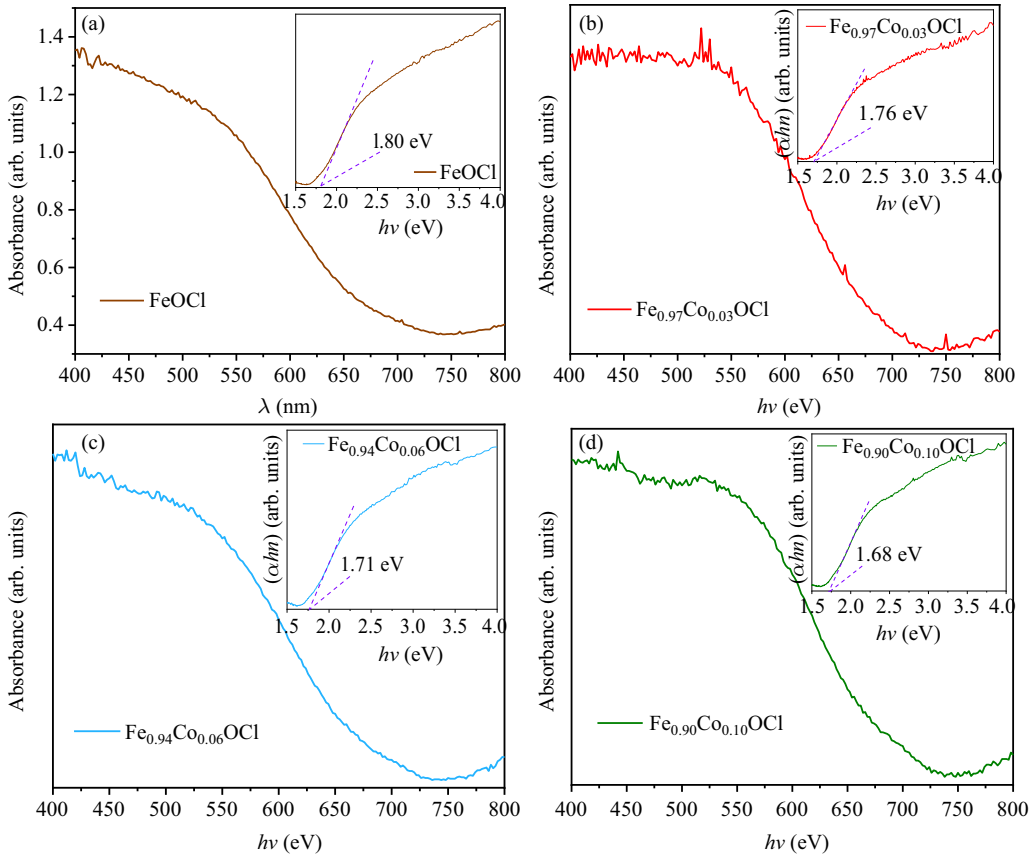


Fig. 9. (a)–(d) UV–visible absorption spectra. The insets show the $(\alpha h\nu)^{1/2}$–$h\nu$ curve of $Fe_{1-x}Co_xOCl$.

Table 1. Bandgap, degradation percentage of the dye after 50 min of reaction and the apparent first-order reaction rate constant for the photo-Fenton process over a $Fe_{1-x}Co_xOCl$ nanosheet.

Sample	Energy gap (eV)	Photo-Fenton degradation (%)	K_{app} (h^{-1})
FeOCl	1.80	81.3	0.0439
$Fe_{0.97}Co_{0.03}OCl$	1.76	89.6	0.0654
$Fe_{0.94}Co_{0.06}OCl$	1.71	98.2	0.0760
$Fe_{0.91}Co_{0.10}OCl$	1.68	87.7	0.0730

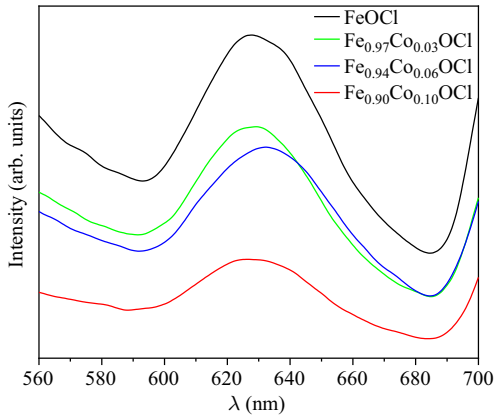


Fig. 10. PL spectrum of $Fe_{1-x}Co_xOCl$.

Figure 10 shows the photoluminescence spectra of $Fe_{1-x}Co_xOCl$ with an excitation wavelength of 503 nm at room temperature. The figure demonstrates that there is a strong emission peak between 600 nm and 650 nm, and the orange–red light corresponds to a transition from a Fe vacancy energy level to an O or Cl. The intensity of the emission peak decreases with increase in the Co ion concentration. The impurity level introduced by Co ion doping is thought to be the cause of this phenomenon.

3.3. DFT calculations

To calculate the band structure of FeOCl and $Fe_{0.94}Co_{0.06}OCl$, the Fermi level was set to 0 the *k*-points were $(2 \times 2 \times 1)$, the kinetic energy cutoff was 400 eV and the convergence criteria for energy and atomic forces were, respectively, 10^{-5} eV/atom and 0.03 eV·Å^{-1}. It was demonstrated unequivocally that the maximum of the valence band (VB) and the minimum of the conduction band (CB) in the reciprocal space are the *G* and *R* points, respectively. Hence, it could be judged that FeOCl and $Fe_{0.94}Co_{0.06}OCl$ are both indirect bandgap semiconductors. The calculated bandgaps of FeOCl and $Fe_{0.94}Co_{0.06}OCl$ are about 1.76 eV and 1.66 eV, which are slightly less than those determined by UV–visible absorption measurement. This is primarily because the DFT calculation is an approximation that uses one electron, making it easy to underestimate the bandgap value. The density of states analysis (Figs. 11(b) and 11(d)) shows that the electronic states pass through the Fermi level of both spin components, suggesting metallic features and enhanced conductivity. It can be seen from the figure that the material has two states after spin polarization: semiconducting in spin-up and metallic in spin-down. The excellent activity of the material is due to the fact that spin polarization leads to different d-bands.

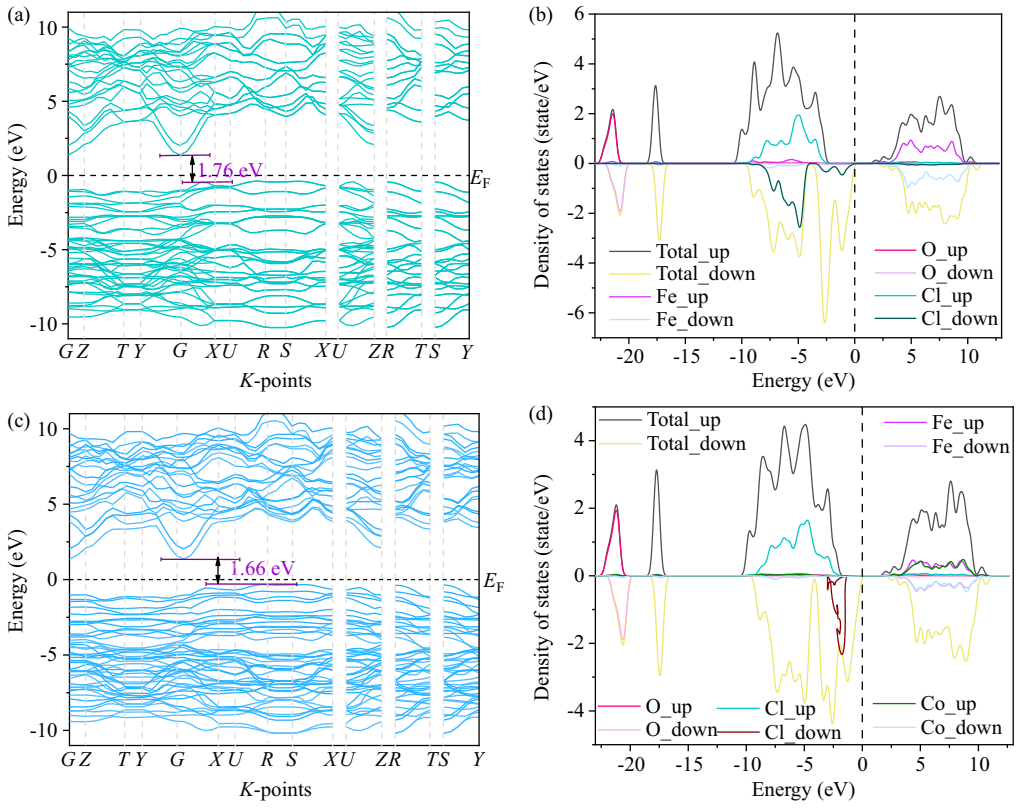


Fig. 11. Calculated band structure and density of states of [(a) and (b)] FeOCl and [(c) and (d)] $Fe_{0.94}Co_{0.06}OCl$.

3.4. Photocatalytic and photo-Fenton performances for RhB

The photocatalytic activity of the as-obtained catalysts was evaluated based on the degradation of 10 mg·l^{-1} aqueous RhB solution under visible-light illumination. Adsorption–desorption equilibrium was realized between the catalysts and RhB after adsorbing for 30 min in the dark. It was found that Co-doped FeOCl significantly increased the adsorption capacity. Figure 12(a) represents the degradation of RhB as a function of reaction time in various photocatalytic processes. There is no significant decolorization of RhB under simulated sunlight illumination without the catalyst, indicating that RhB is stable under visible light. RhB is only slightly degraded during the photocatalytic process with FeOCl, which illustrates the weak photocatalytic performance of FeOCl. Figure 12(c) exhibits the photo-Fenton performance of the synthesized materials in the removal of RhB under visible light, affirming that the removal of RhB can be attributed to combined action by photocatalytic, photo-Fenton and adsorption processes. When FeOCl, $Fe_{0.97}Co_{0.03}OCl$, $Fe_{0.94}Co_{0.06}OCl$ and $Fe_{0.90}Co_{0.10}OCl$ are applied as photo-Fenton catalysts, the degradation rates of RhB are 81.3%, 89.6%, 98.2% and 87.7% over 50 min, respectively. In short, Co doping obviously improves the photocatalytic performance of FeOCl. In addition, the photocatalytic and photo-Fenton degradation process was fitted by first-order kinetics

$$\ln(C_0/C_t) = kt, \tag{2}$$

where C_0 is the initial solution concentration, C_t is the solution concentration at time t and k is the reaction rate constant. As shown in Figs. 12(b) and 12(d), the material shows good linearity, and the photocatalytic and photo-Fenton constants of $Fe_{0.94}Co_{0.06}OCl$ are 11.28 and 1.73 times that of FeOCl. Therefore, the doping of FeOCl with Co effectively improves the photocatalytic and photo-Fenton properties of FeOCl, especially the photocatalytic performance.

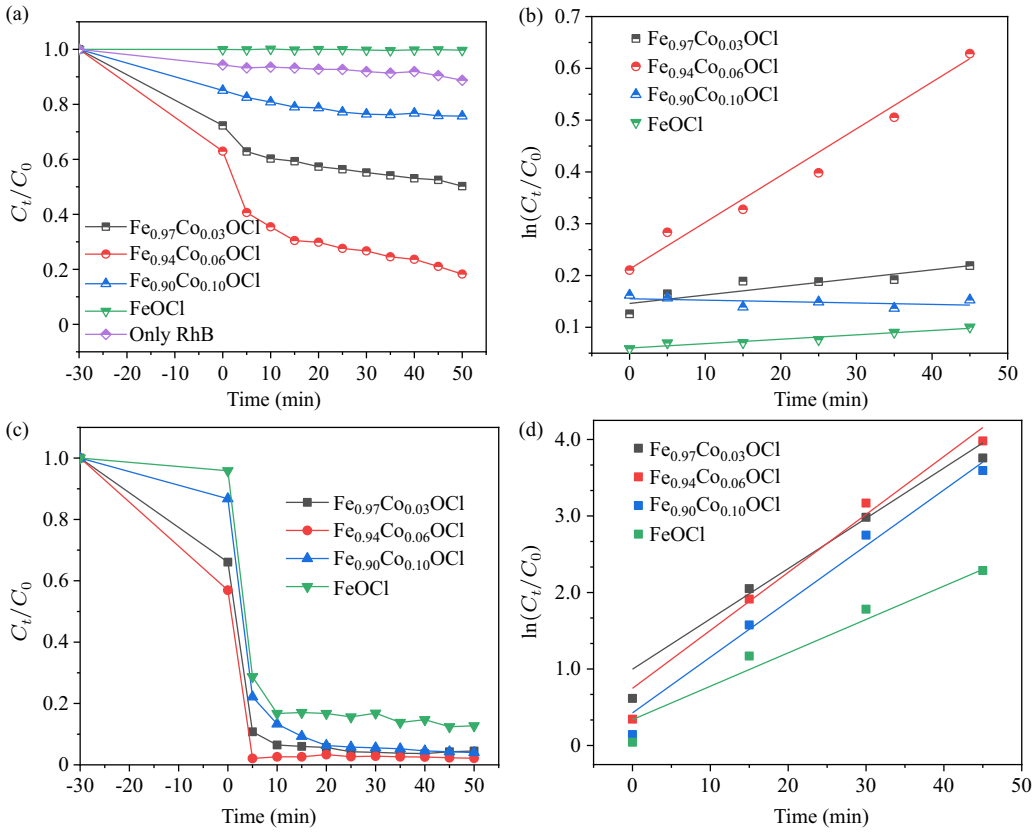


Fig. 12. (a) Photocatalytic degradation, (c) photo-Fenton degradation and [(b) and (d)] the corresponding kinetic plots over $Fe_{1-x}Co_xOCl$.

In order to study the radicals that play a major role in RhB degradation, IPA, IA and BQ were added to the photo-Fenton experiment with $Fe_{0.94}Co_{0.06}OCl$. IPA, IA and BQ are known to be effective inhibitors of ·OH, h^+ and $\cdot O_2^-$ radicals. In Fig. 13(a), the addition of IPA reduced the degradation rate of RhB from 98% to 90%, the presence of IA had almost the same effect as IPA, and BQ had hardly any effect on the experiment. This shows that ·OH and h^+ are the main active species and the $\cdot O_2^-$ radical plays a secondary role. This further indicates that modified $Fe_{0.94}Co_{0.06}OCl$ has higher carrier separation efficiency. The catalyst was collected after the photo-Fenton experiment to test the catalyst's ability to be recycled. The catalyst was washed with deionized water many times and reused after drying. In this paper, five cycle experiments were carried out and it was found that the rate of removal of RhB decreased from 99.8% in the first cycle to 84.5% in the fifth

cycle (Fig. 13(b)). In short, it can be seen from the cyclic experiment that $Fe_{0.94}Co_{0.06}OCl$ could potentially be reused.

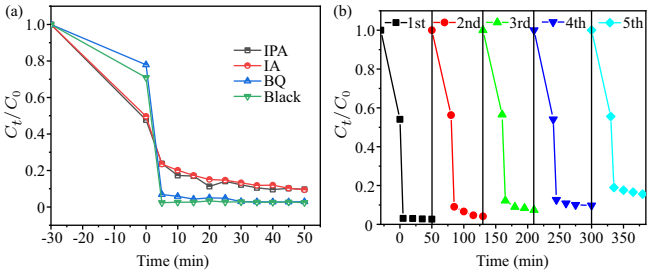


Fig. 13. (a) Effects of different capture agents and (b) recyclability of five runs in the presence of $Fe_{0.94}Co_{0.06}OCl$.

The XRD pattern and SEM image of $Fe_{0.94}Co_{0.06}OCl$ catalyst for RhB photo-Fenton degradation are displayed in Figs. 14(a) and 14(b). There is no obvious shift or additional peaks, showing that the crystal phase structure of $Fe_{0.94}Co_{0.06}OCl$ remained unchanged. But the peak intensity is significantly weaker, showing that the crystallinity of the catalyst changes obviously. This result is also seen in the SEM images of FeOCl, whose morphology is highly aggregated. It is also the reason why the degradation rate of RhB decreases from 98% to 82%.

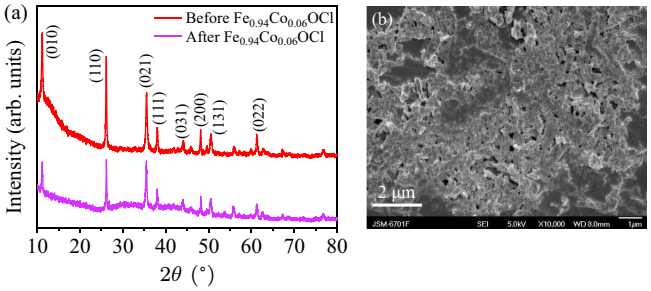


Fig. 14. (a) XRD patterns and (b) SEM images of $Fe_{0.94}Co_{0.06}OCl$ photocatalyst before and after the photo-Fenton degradation experiment.

3.5. Possible photo-Fenton mechanism

Based on the results of the aforementioned analysis, the mechanism of RhB degradation by $Fe_{0.94}Co_{0.06}OCl$ was drawn as shown in Fig. 15. The excellent photocatalytic and photo-Fenton properties of the modified materials under neutral conditions are attributed to the following aspects. First, the Co doping introduces an impurity energy level, which broadens the photoresponse range and provides more trapping centers for carriers. These electrons accelerate the cycling reaction between Fe^{3+} and Fe^{2+}. Second, because Co is a transition metal like Fe, the cycling of Co^{2+}/Co^{3+} ions also produced more ·OH and h^+. The existence of Co^{2+} and Co^{3+} in $Fe_{0.94}Co_{0.06}OCl$ has been proved by XPS. Finally, based on previous research to confirm the VB potential of FeOCl and $Fe_{0.94}Co_{0.06}OCl$, the VB spectrum was measured and the results were about 2.47 eV and 2.44 eV. The energy band edge position of the CB of the FeOCl and $Fe_{0.94}Co_{0.06}OCl$ nanoparticles was determined by the following equation:

$$E_{VB} = E_{CB} + E_g, \tag{3}$$

where E_g is the sample band gap. The conduction bands of FeOCl and $Fe_{0.94}Co_{0.06}OCl$ nanosheets by calculation are 0.67 eV and 0.73 eV.

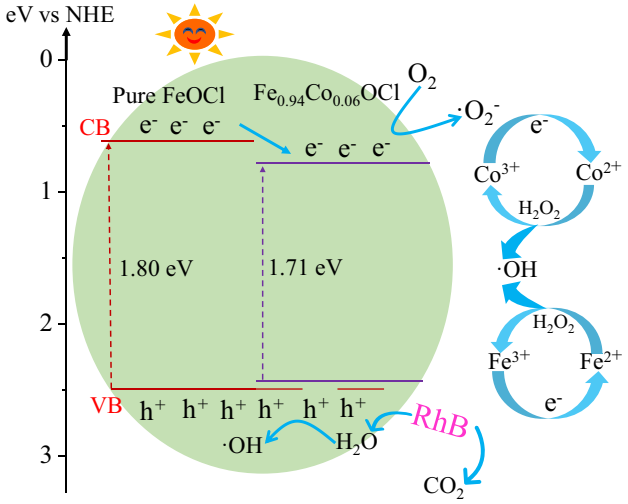


Fig. 15. Catalytic mechanism in the $Fe_{0.94}Co_{0.06}OCl$ system (vs NHE: versus normal hydrogen electrode).

The entire catalytic degradation process of RhB is expressed in several formulae. When the catalyst semiconductor is subjected to energy ($h\nu$) ≥ bandgap energy (E_g), the electron–hole pairs on the catalyst surface are activated (Eq. (4)).[42] Some of the electrons in the conduction band will capture O_2 to form O_2^- (Eq. (5)), and $\cdot O_2^-$ reacts with H_2O_2 to form OH (Eq. (7)). This is the reason why O_2^- is not the main active species,[43] and other electrons participated in the cycling experiment of Fe^{3+}/Fe^{2+} (Eq. (10)) and Co^{3+}/Co^{2+} (Eq. (11)) ions. In this process, a large amount of h^+ is produced and some of the of h^+ adsorb H_2O to generate ·OH (Eq. (6)). H_2O_2 mainly oxidizes Fe^{2+} and Co^{2+} into Fe^{3+} and Co^{3+} (Eqs. (8) and (9)), producing a large amount of ·OH. This result is consistent with that of the radical capture experiment. Therefore, RhB is degraded into small inorganic molecules such as H_2O and CO_2 by ·OH, h^+ and a few $\cdot O_2^-$ active species (Eq. (12)):

$$Fe_{1-x}Co_xOCl + h\nu \rightarrow e^- + h^+, \tag{4}$$

$$e^- + O_2 \rightarrow \cdot O_2^-, \tag{5}$$

$$h^+ + H_2O \rightarrow \cdot OH + H^+, \tag{6}$$

$$H_2O_2 + \cdot O_2^- \rightarrow \cdot OH + OH^- + O_2, \tag{7}$$

$$Fe^{3+} + e^- \rightarrow Fe^{2+}, \tag{8}$$

$$Co^{3+} + e^- \rightarrow Co^{2+}, \tag{9}$$

$$Fe^{2+} + H_2O_2 \rightarrow Fe^{3+} + \cdot OH + OH^-, \tag{10}$$

$$Co^{2+} + H_2O_2 \rightarrow Co^{3+} + \cdot OH + OH^-, \tag{11}$$

$$\cdot OH + h^+ + \cdot O_2^- + RhB \rightarrow CO_2 + H_2O. \tag{12}$$

4. Conclusion

In conclusion, using the one-step calcination method, a series of $Fe_{1-x}Co_xOCl$ catalysts were successfully synthesized. EDS and TEM mapping results showed that the prepared complexes contained Co. XPS characterization results further indicated that Co ions exist in divalent and trivalent states like Fe ions. Additionally, when the $Fe_{1-x}Co_xOCl$ underwent a photo-Fenton reaction it was discovered that $Fe_{0.94}Co_{0.06}OCl$ had exceptional catalytic capabilities in neutral solution at ambient temperature and under visible light. This was further illustrated by the increased density of photogenerated carriers found by PL characterization and DFT calculations. Most importantly, this doping method not only changes the photocatalytic performance of FeOCl, but also changes the cycling stability of FeOCl.

Acknowledgments

Project supported by the National Natural Science Foundation of China (Grant No. 52268042), the Natural Science Foundation of Gansu Province, China (Grant No. 22JR5RA253), and HongLiu First-Class Disciplines Development Program of Lanzhou University of Technology.

References

[1] Ashouri M J and Rafei M 2018 *Environ. Sci. Poll. Res.* **25** 17590
[2] Huang S P, Wei Z Q, Ding M J, Li C and Lu Q 2021 *Opt. Mater.* **111** 110643
[3] Li C, Wei Z Q, Lu Q, Ma J H and Li L 2022 *Environ. Sci. Poll. Res.* **29** 34930
[4] Yang Y, Li X, Zhou C Y, Xiong W P and Zeng G M 2020 *Water Research* **184** 116200
[5] Zamanzad-Ghavidel S, Sobhani R, Etaei S, Hosseini Z and Montaseri M 2021 *Environ. Monitor. Assess.* **193** 463
[6] Zhang D, Zhu M Y, Yu J G, Meng H W and Jiao F P 2017 *T. Nonferr. Metal. Soc.* **27** 2673
[7] Brillas E and Garcia-Segura S 2020 *Sep. Purif. Technol.* **237** 116337
[8] Jiang Y N, Xiong Z K, Huang J B, Yan F, Yao G and Lai B 2022 *Chin. Chem. Lett.* **33** 415
[9] Zhao W, Wei Z, Ma L, Liang J and Zhang X 2019 *Materials* **12** 582
[10] Li H B, Huang G Y, Zhang J, Fu S H, Wang T G and Liao H W 2017 *T. Nonferr. Metal. Soc.* **27** 1127
[11] Zheng Y S, Qiu S, Deng F X, Zhu Y S, Ma F and Li GJ 2021 *Environ. Tech.* **42** 1996
[12] Ma J H, Wei Z Q, Li L, Ma L, Li C and Huang S P 2021 *Desalin. Water Treat.* **231** 287
[13] Tong X, Jia W J, Li Y M, Yao T J, Wu J and Yang M 2019 *J. Taiwan Inst. Chem. E* **102** 92
[14] Sales H B, Menezes R R, Neves G A, de Souza J J N and Ferreira J M 2020 *Sustainability* **12** 7393
[15] Li L, Lai C, Huang F L, Cheng M and Zeng G M 2019 *Water Res.* **160** 238
[16] Fu S M, Li G S, Wen X, Fan C M and Liu J X 2020 *Trans. Nonferr. Metals Soc. China* **30** 765
[17] Xu Q L, Zhang L Y, Cheng B, Fan J J and Yu J G 2020 *Chem* **6** 1543
[18] Yang J, Huang Z, Yang B D, Lin H and Qin L Z 2021 *J. Mater. Sci.* **56** 3268
[19] Xing M Y, Xu W J, Dong C C, Bai Y C and Zeng J B 2018 *Chem* **4** 1359
[20] Zhang B F, Zhang L, Akiyama K, Bingham P A, Zhou Y T and Kubuki S 2021 *Acs Appl. Mater. Inter.* **13** 22694
[21] Liu F, Yao H, Sun S B, Tao W J, Wei T and Sun P Z 2020 *Chem. Eng. J.* **402** 125477
[22] Guo T, Wang K, Zhang G K and Wu X Y 2019 *Appl. Surf. Sci.* **469** 331
[23] Yang L, Li L, Liu Z T, Lai C and Yang X F 2022 *Chemosphere* **294** 133736
[24] Yang M, Liu J, Xu H, Pei Y and Jiang C 2022 *ChemPhysMater* **1** 155
[25] Sun B, He D, Wang H B, Liu J C and Ke Z J 2021 *Chin. Phys. B* **30** 106102
[26] Ji X X, Wang H F and Hu P J 2019 *Rare. Metal.* **38** 783
[27] Setyawan W and Curtarolo S 2010 *Com. Mater. Sci.* **49** 299
[28] Zhao J Z, Ji M X, Di J, Zhang Y and He M Q 2020 *J. Photoch. Photobio. A* **391** 112343
[29] Chen Y Q, Liu Y P, Zhang L, Xie P C and Wang Z P 2018 *J. Hazard Mater.* **353** 18
[30] Shi X H, Cui C, Zhang L, Zhang J and Liu GD 2019 *New J. Chem.* **43** 16273
[31] Wang L, Yang H, Kang L, Wu M and Yang Y 2022 *Chemosphere* **296** 134039
[32] Zhang J, Liu G D and Liu S J 2018 *New J. Chem.* **42** 6896
[33] Sun S B, Yao H, Fu W Y, Liu F, Wang X W and Zhang W 2021 *J. Environ. Chem. Eng.* **9** 104501
[34] Nguyen T B, Huang C P, Doong R A, Chen C W and Dong C D 2021 *J. Hazard. Mater.* **401** 123326
[35] Asadzadeh-Khaneghah S, Habibi-Yangjeh A, Seifzadeh D, Chand H, Krishnan V 2021 *Colloid. Surface A* **617** 126424
[36] Jiang L L, Zhang L, Cui C, Zhang J, Liu G D and Song J J 2019 *Mater. Lett.* **240** 30
[37] Liu X, Zhang W Y, Peng M G, Zhai G Q, Hu L C and Mao L Q 2021 *Chem. Eng. J* **426** 131353
[38] Chen M D, Xu H M, Wang Q, Li D Y and Xia D S 2018 *Chem. Phys. Lett.* **706** 415
[39] Wei J S, Feng X, Hu X F, Yang J H, Yang C and Liu B Y 2021 *Colloid. Surf. A* **631** 127754
[40] Zhang J, Yang M X, Lian Y, Zhong M L and Sha J Q 2019 *Dalton. T.* **48** 3476
[41] Zhong X, Zhang K X, Wu D, Ye X Y, Huang W and Zhou B X 2020 *Chem. Eng. J.* **383** 123148
[42] Kumar A and Luxmi V 2020 *Optik* **216** 164804
[43] Gao J, Liu Y, Xia X, Wang L and Shao L 2019 *Appl. Surf. Sci.* **463** 863